The Astrophysical Journal, 834:36 (10pp), 2017 January 1 doi:10.3847/1538-4357/834/1/36

THE LOCAL [C II] 158 μm EMISSION LINE LUMINOSITY FUNCTION

Shoubaneh Hemmati[1], Lin Yan[1], Tanio Diaz-Santos[2], Lee Armus[3], Peter Capak[1,3], Andreas Faisst[1], and Daniel Masters[1]
[1] Infrared Processing and Analysis Center, Department of Astronomy, California Institute of Technology, 1200 E. California Boulevard, Pasadena CA 91125, USA; shemmati@ipac.caltech.edu
[2] Nucleo de Astronomia de la Facultad de Ingenieria, Universidad Diego Portales, Avenue Ejercito Libertador 441, Santiago, Chile
[3] Spitzer Science Center, Department of Astronomy, California Institute of Technology, 1200 E. California Boulevard, Pasadena, CA 91125, USA
Received 2016 July 22; revised 2016 November 7; accepted 2016 November 9; published 2016 December 28

ABSTRACT

We present, for the first time, the local [C II] 158 μm emission line luminosity function measured using a sample of more than 500 galaxies from the Revised Bright Galaxy Sample. [C II] luminosities are measured from the *Herschel* PACS observations of the Luminous Infrared Galaxies (LIRGs) in the Great Observatories All-sky LIRG Survey and estimated for the rest of the sample based on the far-infrared (far-IR) luminosity and color. The sample covers 91.3% of the sky and is complete at $S_{60\,\mu\mathrm{m}} > 5.24$ Jy. We calculate the completeness as a function of [C II] line luminosity and distance, based on the far-IR color and flux densities. The [C II] luminosity function is constrained in the range $\sim 10^{7-9}\,L_{\odot}$ from both the $1/V_{\max}$ and a maximum likelihood methods. The shape of our derived [C II] emission line luminosity function agrees well with the IR luminosity function. For the CO(1-0) and [C II] luminosity functions to agree, we propose a varying ratio of [C II]/CO(1-0) as a function of CO luminosity, with larger ratios for fainter CO luminosities. Limited [C II] high-redshift observations as well as estimates based on the IR and UV luminosity functions are suggestive of an evolution in the [C II] luminosity function similar to the evolution trend of the cosmic star formation rate density. Deep surveys using the Atacama Large Millimeter Array with full capability will be able to confirm this prediction.

Key words: galaxies: evolution – galaxies: luminosity function, mass function – infrared: galaxies – quasars: emission lines

1. INTRODUCTION

The gas content in the interstellar medium (ISM) of galaxies is critical in galaxy evolution, serving as the immediate fuel for star formation (Scoville et al. 2016). Rotational transitions of common interstellar molecules, such as CO, as well as atomic fine-structure line transitions, predominantly [C II], can be used to study the amount and distribution of the cold gas content in galaxies (e.g., Carilli & Walter 2013).

The [C II] fine-structure line at 157.74 μm, which arises from the transition of singly ionized carbon atoms (C^+) from the $^2P_{3/2}$ to the $^2P_{1/2}$ state, is the strongest emission line in the far-infrared (far-IR). The primary mechanism for producing this line is excitation of C^+ atoms via collisions with other particles such as neutral hydrogen (H) or free electrons and protons (e.g., Hayes & Nussbaumer 1984). The ionization potential of C^+ is quite shallow, only 11.26 eV, and the critical density of collisions with neutral and molecular hydrogen $n_{\mathrm{H}}^{\mathrm{cr}}$ is also small, for $T = 100k \sim 3 \times 10^3$ cm^{-3} (Goldsmith et al. 2012). Therefore, the 158 μm line is an efficient and dominating coolant for neutral gas. For nearby normal star-forming galaxies as well as Luminous Infrared Galaxies (LIRGs), the 158 μm line, in combination with far-IR continuum, CO (1-0), and [N II], provides powerful spectral diagnostics of the physical state of the ISM, such as the intensity of the far-UV radiation field, temperature, density and chemical abundance (e.g., Malhotra et al. 1997; Kaufman et al. 1999; Stacey et al. 2010; Nagao et al. 2012). [C II] emission can be produced in both neutral as well as ionized phases of the ISM. For example, in the Milky Way, Pineda et al. (2014) measured the contribution of the ionized phase of the ISM to [C II] luminosity to be around 20% and the remaining 80% coming from the neutral gas. Goldsmith et al. (2015) showed that the contribution from the ionized region can be as high as 50% using PACS observations of ionized nitrogen in the Galactic plane. In other galaxies, the fraction of [C II] arising from the ionized regions compared to neutral parts is more uncertain and still a matter of study. It has been shown to vary for different galaxies and to depend on the properties of the ISM (e.g., Cormier et al. 2012; Decarli et al. 2014; Gullberg et al. 2015; Olsen et al. 2015).

Many studies have focused on the [C II] emission line luminosity as a star formation rate indicator, as it is a very bright line almost unaffected by extinction (e.g., Stacey et al. 1991; Boselli et al. 2002; Graciá-Carpio et al. 2011; Sargsyan et al. 2012; De Looze et al. 2014; Brisbin et al. 2015; Vallini et al. 2015). The major limitation for using the [C II] luminosity to measure the star formation rate is the so-called [C II] deficit, which corresponds to a lower fraction of [C II] to far-IR as a function of increasing warm IR color (e.g., Malhotra et al. 1997, 2001, Díaz-Santos et al. 2013). More recently, Díaz-Santos et al. (2014), using a sample of luminous local LIRGs, found that the [C II] deficits are restricted to their nuclei. Herrera-Camus et al. (2015), using the resolved [C II] observations of *Herschel* KINGFISH (Kennicutt et al. 2011) galaxies, also showed that the [C II] surface density correlates well with star formation rate surface density both globally and in the kpc scale in the absence of strong active galactic nuclei.

Over the next few years, with its steadily improved sensitivity and frequency coverage, the Atacama Large Millimeter Array (ALMA) will dramatically increase the number of galaxies with detected [C II] emission at high redshift (e.g., Swinbank et al. 2012, Capak et al. 2015; Aravena et al. 2016), making systematic surveys possible. One powerful

application of [C II], the brightest of far-IR emission lines, is for measuring redshifts of distant ($z \geqslant 6$) galaxies in the early universe. Similar to commonly seen galaxy redshift surveys based on optical spectroscopy, these ALMA [C II] surveys will characterize the abundance and intensity distributions of [C II] emitters by deriving the line luminosity functions. Future [C II] redshift surveys would require a well-measured line luminosity function at $z \sim 0$ for comparison.

Previous studies have briefly looked at the [C II] line local luminosity function using either far-IR luminosity functions or limited luminosity range observed data with complex selection functions (e.g., Brauher et al. 2008; Swinbank et al. 2012). The goal of this paper is to obtain the $z \sim 0$ [C II] luminosity function benchmark. The *Herschel* space observatory (Pilbratt et al. 2010), with its sensitive far-IR spectroscopy and fast survey speed, has produced large samples of galaxies with [C II] detections at various redshifts (e.g., Díaz-Santos et al. 2013; Farrah et al. 2013; Herrera-Camus et al. 2015). In the local universe, the far-IR spectra of a complete sample of Luminous/Ultraluminous Infrared Galaxies (LIRGs/ULIRGs) from the Great Observatories All-sky LIRG Survey (GOALS) (Armus et al. 2009; Díaz-Santos et al. 2013) is the primary data set we use for our analysis because it is a complete set of [C II] observations of the Revised Bright Galaxy Sample (RBGS; Sanders et al. 2003). In Section 2 we discuss in detail the selection of the local sample and its completeness. We present the local [C II] line luminosity function in Section 3. We discuss and compare our results to other indirect methods of estimating the [C II] line luminosity function in the local universe and also predicts the evolution of [C II] line luminosity function from existing UV observations in Section 4. The summary of the paper is presented in Section 5. Throughout the paper, we adopt a flat concordance ΛCDM cosmology, with $\Omega_m = 0.28$, $\Omega_\Lambda = 0.72$, and $H_0 = 70$ km s^{-1} Mpc^{-1}.

2. SAMPLE

The most ideal survey for [C II] line luminosity function is a blind spectroscopic survey with a uniform flux sensitivity, covering a well defined area of sky. In reality, such a survey with far-IR spectroscopy over a large area is not possible, especially at $z \sim 0$. The next best available option is to utilize the [C II] observations of a complete sample of local galaxies with a well defined selection function. The RBGS sample contains a total of 629 galaxies and is a complete 60 μm flux-limited sample of all galaxies satisfying the following criteria: (1) *IRAS* flux density $S_{60\,\mu\mathrm{m}} > 5.24$ Jy; (2) galactic latitudes $|b| > 5°$. GOALS (Armus et al. 2009) contains all (202) LIRGs $L_{8-1000\,\mu\mathrm{m}} \geqslant 10^{11}\,L_\odot$ in the RBGS. All GOALS sources have complete far-IR photometric and spectroscopic coverage from *IRAS*, *Spitzer,* and *Herschel*.

The GOALS sample was observed by the Integral Field Spectrometer of the PACS instrument (Poglitsch et al. 2010) on board *Herschel*. For this paper, we took the best [C II] 158 μm line measurement from a variety of apertures depending on each individual source (T. Diaz-Santos et al. 2016, in preparation). In short, the best measurement is chosen based on visual inspection of each individual source. In most cases we have used the total field of view (FOV) (5 × 5 spaxel) quantities; in a few cases where two components were resolved within the FOV, the central spaxel (corrected for aperture) was used instead. Díaz-Santos et al. (2013, 2014) give a detailed description on how the data were reduced and the [C II] 158 μm line fluxes were measured. In short, the *Herschel* Interactive Processing Environment (ver. 8.0) application was used to retrieve and process the spectra. The [C II] flux is then measured by integrating the continuum-subtracted spectrum within the $\pm 3\sigma$ region around the central position of the line, and the associated uncertainty is calculated as the standard deviation of the continuum integrated over the same range of the line. The major portion of this far-IR spectroscopic data set is from the program Herschel OT1_larmus, and the remainder is from public archive data, collected by three other programs (KPGT_esturm_1, PI: E. Sturm; KPOT_pvanderw_1, PI: P. van der Werf; OT1_dweedman_1, PI: D. Weedman). Of the 202 (U)LIRGs from the GOALS sample, 200 have [C II] observations (IRAS F08339+6517 and IRAS F09111-1007 have no PACS spectra).

2.1. [C II] Luminosities and Uncertainties

Ideally, constraining the [C II] line luminosity function down to faint luminosities ($\sim 10^{(7-8)}\,L_\odot$), would require far-IR spectroscopy of a complete sample of low IR luminosity galaxies. However, such a data set currently does not exist. The alternative best approach is to predict the [C II] luminosities for RBGS galaxies fainter than LIRGS in the GOALS sample ($L_{\mathrm{IR}} < 10^{11}\,L_\odot$). The [C II] luminosities are calculated using the established correlation between $f([\mathrm{C\,II}])/f(\mathrm{FIR})$ versus far-IR color, e.g., dust temperature (T_{dust}) (see Díaz-Santos et al. (2013) and references therein). This relation, as shown on the left panel of Figure 1, is expressed as:

$$\frac{[\mathrm{C\,II}]}{\mathrm{FIR}} = 0.016(\pm 0.001) \times \exp\left(\frac{\frac{S_{63\,\mu\mathrm{m}}}{S_{158\,\mu\mathrm{m}}}}{0.60(\pm 0.038)}\right) \quad (1)$$

with a dispersion of 0.0017 dex. We used a modified blackbody function with an emissivity index of $\beta = 1.8$ and reference wavelength of 100 μm, that reproduces the observed $S_{63\,\mu\mathrm{m}}/S_{158\,\mu\mathrm{m}}$ color with the dust temperature shown in the upper axis of Figure 1. The far-IR fluxes covering the 40–500 μm are calculated as: FIR $= 1.26 \times 10^{-14}(2.58 S_{60\,\mu\mathrm{m}} + S_{100\,\mu\mathrm{m}})[\mathrm{W\,m^{-2}}]$ (Helou et al. 2000) where S_ν are in [Jy]. To measure the far-IR color on the right-hand side of Equation (1), we use the correlation between the PACS-based far-IR color $S_{63\,\mu\mathrm{m}}/S_{158\,\mu\mathrm{m}}$ and the more commonly used *IRAS*-based color $S_{60\,\mu\mathrm{m}}/S_{100\,\mu\mathrm{m}}$.

$$\mathrm{Log}\left(\frac{S_{60\,\mu\mathrm{m}}}{S_{100\,\mu\mathrm{m}}}\right) = -0.161(\pm 0.004) + 0.539(\pm 0.018) \times \mathrm{Log}\left(\frac{S_{63\,\mu\mathrm{m}}}{S_{158\,\mu\mathrm{m}}}\right) \quad (2)$$

As expected, and shown on the right panel of Figure 1, the two colors correlate well, with a dispersion of 0.052 dex.

The 1σ uncertainties of [C II] luminosities for GOALS galaxies are taken from Díaz-Santos et al. (2014). For the non-GOALS RBGS galaxies, however, all the above-mentioned assumptions need to be accounted for. We calculate these errors using a bootstrapping technique. We perturb $S_{60\,\mu\mathrm{m}}$, $S_{100\,\mu\mathrm{m}}$ flux densities far-IR fluxes as well as the fitting parameters (from Equations (1) and (2)) by randomly drawing values from normal distributions with their corresponding

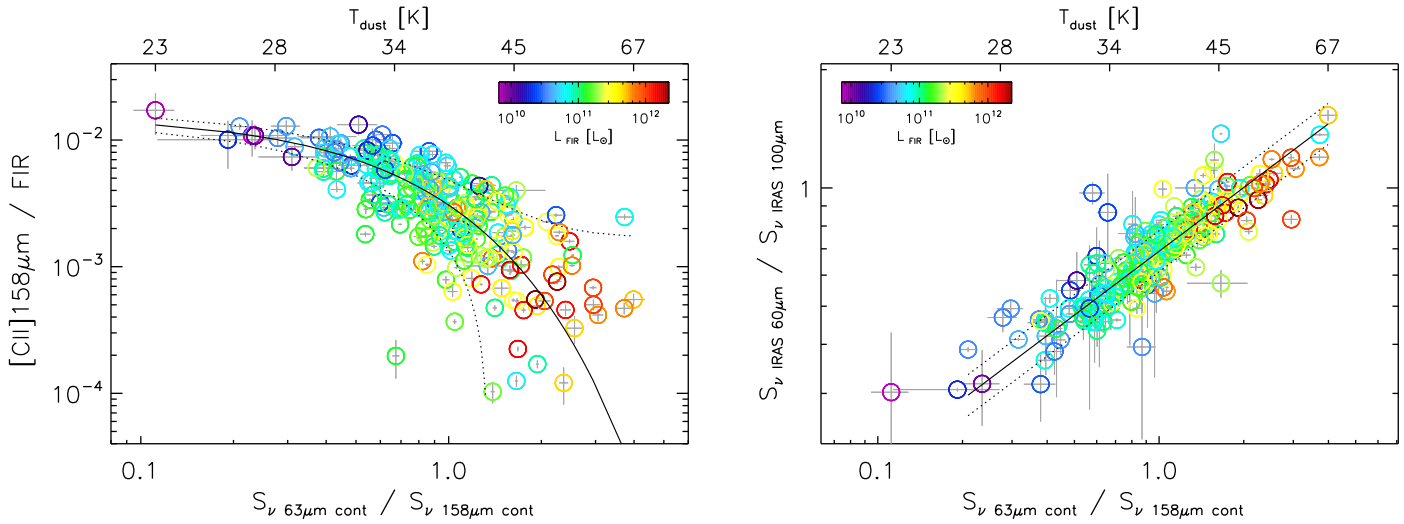

Figure 1. (Left) $f([\mathrm{C\,II}])/f(\mathrm{FIR})$ vs. far-IR color $S_{63\,\mu m}/S_{158\,\mu m}$ of the galaxies in the GOALS sample color-coded by the IR luminosity and (right) *IRAS*-based far-IR color $S_{60\,\mu m}/S_{100\,\mu m}$ vs. the PACS based color $S_{63\,\mu m}/S_{158\,\mu m}$. The solid and dashed black lines corresponding to the best fitted relation and 1σ dispersion are used to predict the [C II] line luminosity for the rest of the RBGS sample.

standard errors as widths of the distributions to measure the [C II] line luminosity standard error. These 1σ measured uncertainties are largely dominated by the uncertainties in the fitted parameters in Equations (1) and (2) and are an upper limit to the true error as the uncertainty in the fitting parameters already account for uncertainties in fluxes and flux densities. Our method allows us to quantify the uncertainties in the derived [C II] luminosities for non-GOALs galaxies. Fundamentally, these uncertainties are driven by the intrinsic variations in [C II]-to-FIR flux ratios. [C II]-to-FIR ratios are affected by several physical conditions, such as far-IR temperature, neutral gas density, or equivalently surface brightness (e.g., Lutz et al. 2016). [C II] emission is collisionally excited and can be suppressed in very high-density regions. Another possible physical process leading to [C II] deficit is the reduction in the photoelectric heating efficiency due to the charging of the dust grains. Therefore, the scattering in the observed [C II]/FIR versus $S_{63\,\mu m}/S_{158\,\mu m}$ relation reflects the physical diversity of ISM in different galaxies.

After excluding the very nearby galaxies (luminosity distances less than 1 Mpc) as well as those with predicted [C II] line luminosity less than the lowest PACS observed [C II] line luminosity ($10^{6.73}\,L_\odot$) from this sample, we are left with 200 GOALS and 395 RBGS non-GOALS galaxies spanning the redshift range of 0.00023–0.076 and [C II] line luminosities in the range $10^{6.73\text{–}9.33}\,L_\odot$

2.2. Completeness

The sample we have selected here is complete at flux density $S_{60\,\mu m} > 5.24$ Jy. However, to estimate the [C II] line luminosity function, we need to know how incomplete the sample is at each [C II] line flux. We therefore calculate a completeness function at each [C II] line flux ($C([\mathrm{C\,II}], D_L)$). This is critical for determining the faint end of the line luminosity function. To estimate the amount of completeness at each [C II] flux, we make a grid of [C II] line luminosity and distance. At each cell of this grid we randomly draw a hundred far-IR colors ($S_{60\mu m}/S_{100\,\mu m}$) and use these ratios along with Equations (1) and (2) and their dispersion as well as the definition of far-IR to calculate the corresponding $S_{60\,\mu m}$. Then the completeness fraction at each cell of the grid is simply the ratio of galaxies with $S_{60\,\mu m} > 5.24$ Jy (the selection criteria for the RBGS) to all 100 galaxies in that grid. The completeness function is shown in the left panel of Figure 2. As we are going to use this completeness function in the luminosity function, to speed up the calculation we fit an analytical form to it. The best-fit function as shown on the right panel of Figure 2 is expressed with a sigmoid function as:

$$C([\mathrm{C\,II}], D_L) = \frac{100}{1 + \exp(-2.4(\mathrm{Log}([\mathrm{C\,II}]) - 4.86(D_L - 4.256)^{0.2}))} \quad (3)$$

where the unit of [C II] luminosities is $L_\odot$ and distances are in Mpc. Completeness for different surveys is often just measured by the turnover in the source counts as a function of brightness. Here, we also show the [C II] line flux at which the source count starts to drop with a white dashed line on Figure 2 which agrees well with where our completeness function starts to drop.

In Figure 2 we also show where our galaxies sit with black crosses (GOALS objects) and plus symbols (the rest of the RBGS) on top of the rainbow-colored completeness values. The galaxies are not originally selected based on their [C II] luminosity and the majority of the sample sits above 80% completeness. We note that the handful of galaxies with completeness values below 50% are all from the GOALS sample with observed [C II] luminosities. The completeness values will be used as weights for probabilities of individual sources in the sample. We explain the details of implementing the completeness in the next section.

In addition to the source detection incompleteness, the sky coverage percentage is also accounted for in our calculation. This galaxy sample spans the entire sky except for a thin strip within a galactic latitude of $|b| < 5°$. The effective sky coverage is 37,657 square degrees, 91.3% of the full sky (Sanders et al. 2003). We include this multiplicative factor in the luminosity function estimation.

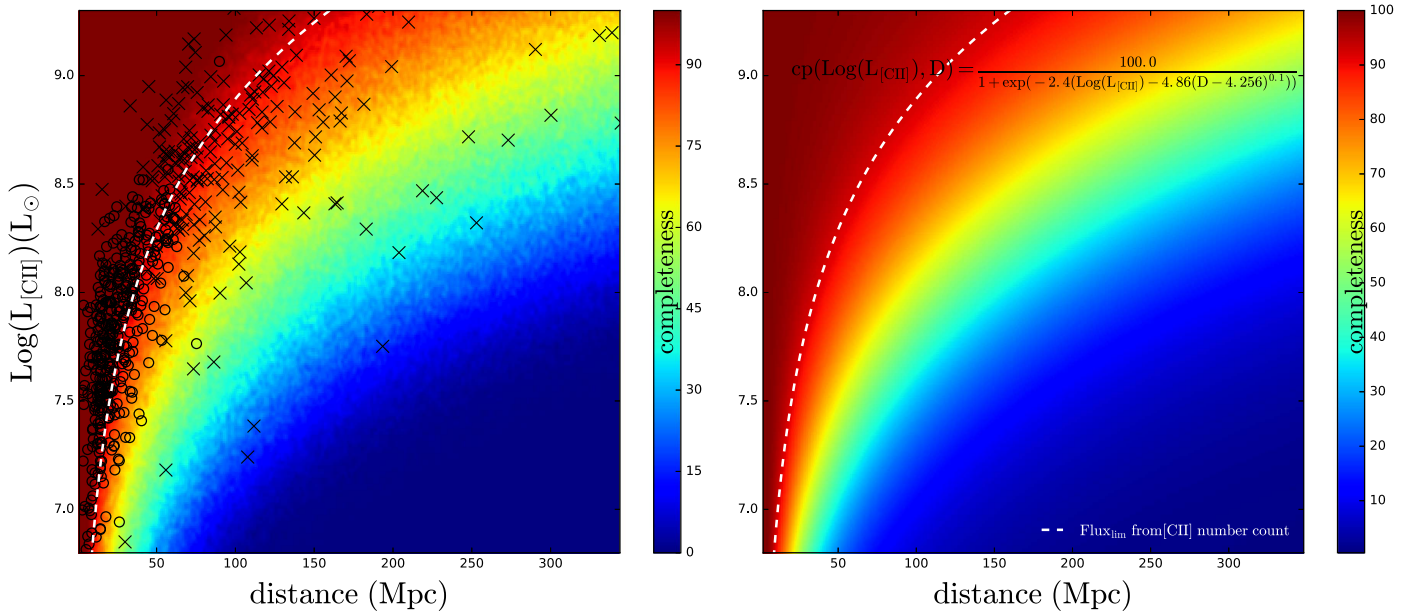

Figure 2. Completeness percentage at each [C II] line luminosity and distance. (Left) Measured numerical values from simulation. (Right) Analytical fitted function. The white dashed line which shows the 100% completeness as measured from the [C II] flux number count turn over agrees very well with this method. Black crosses are our sources from the GOALS survey and black circles are the rest of the sample from the RBGS.

3. LUMINOSITY FUNCTION

Various methods exist for estimating the luminosity function. Each has its own advantages and disadvantages. The most widely used method is the $1/V_{\rm max}$ method (Schmidt 1968; Felten 1976) which assumes no parametric form for the luminosity function and is very easy to implement. However, in this method galaxies are binned into different luminosity bins and the choice of the bin size and centers of the bins might affect the overall shape of the luminosity function. Another well-established method is the maximum likelihood estimator (Sandage et al. 1979) which has the great advantage of using unbinned data. But unlike the $1/V_{\rm max}$ method, here a parametric form for the luminosity function needs to be assumed. Also, the $1/V_{\rm max}$ method is only accurate if there is a uniform density distribution. For large enough surveys such as ours, this is not an issue. Here, we determine the [C II] line luminosity function using both of these methods.

3.1. $1/V_{\rm max}$

We start with the $1/V_{\rm max}$ method to estimate the [C II] line luminosity function. This method was first discussed by Schmidt (1968) and revised later by Felten (1976). With this method, when we calculate the volume number density of galaxies per $\Delta(L)$ for a flux-limited sample, the relevant quantity is the maximum volume ($V_{\rm max}$) within which a galaxy could lie and still be detected by the survey. The underlying concept is that a brighter galaxy can be seen further away than an intrinsically fainter one, thus probing a larger volume. This maximum volume is usually constrained by both the maximum and minimum redshift an object could have and still be included in the survey sample.

The minimum redshift ($z_{\rm min}$) for all the galaxies in the sample is set by the cut on the luminosity distance ($D_L > 1$ Mpc) as mentioned in the previous section. The maximum redshift ($z_{\rm max}$) a galaxy can have and still be included in the sample is the maximum between the galaxy's actual redshift and that measured by comparing the [C II] line flux ($F_{\rm [C\,II]}$) to the limiting line flux ($\rm Flim_{[C\,II]}$) of the sample:

$$z_{\rm max} = \max\left(z,\ 0.5\left(\sqrt{1 + 4z(1+z)\sqrt{\frac{F_{\rm [C\,II]}}{\rm Flim_{[C\,II]}}}} - 1\right)\right). \quad (4)$$

All cosmological calculations, such as co-moving distance and volume, are simplified for galaxies with small redshifts. Here we adopt the following equations: luminosity distance $D_L = z(1+z)\frac{c}{H_0}$; co-moving volume $V_c = \frac{4\pi}{3}D_M^3$, with D_M being proper distance ($\frac{cz}{H_0}$) (Hogg 1999). The co-moving maximum volume for each galaxy in the sample is then calculated as:

$$V_{\rm max} = \frac{4\pi}{3}(D_{\rm M}^3(z_{\rm max}) - D_{\rm M}^3(z_{\rm min})). \quad (5)$$

Finally, the luminosity function is the sum of $(1/V_{{\rm max},i})$ over all galaxies, divided by the luminosity interval of $\rm Log(L_{[C\,II]}) = 0.2\,L_\odot$ with which the luminosity function is binned (Table 2).

$$\phi(L) = \frac{1}{\Delta L}\sum_i \frac{1}{V_{{\rm max},i}}. \quad (6)$$

3.2. Maximum Likelihood Estimator

The maximum likelihood estimator is a powerful tool in statistics which estimates the parameters of a model, given the data. In observational cosmology, it was first used by Sandage et al. (1979) (hereafter STY) for deriving luminosity functions of different types of galaxies. As mentioned earlier, this method assumes a functional form for the luminosity function which elliminates the need for binning the data. The most common model used in UV and optical studies is the Schechter function. This is expected as the model was originally derived from a stellar mass function (Press & Schechter 1974; Schechter 1976). In the IR, however, more galaxies have been found in the bright

end making a double power-law a better fit to the luminosity function (e.g., Soifer et al. 1987, Patel et al. 2013). For our analysis, we tested both functional forms and found that the double power-law is a much better fit to the shape of the luminosity function, defined as:

$$\phi(L) = \phi^*((L/L^*)^{\alpha} + (L/L^*)^{\beta})^{-1} \quad (7)$$

where ϕ^* is the normalization factor, L^* is the characteristic luminosity, and α and β are the slopes of the faint and bright end of the luminosity function. To find the optimized parameters of the double-power-law luminosity function given our [C II] line luminosities and uncertainties, we have to maximize the product ($\mathcal{L}$) of probabilities of finding each galaxy in the sample:

$$\mathcal{L} = \prod_i P(L_i|\alpha, \beta, L^*) \quad (8)$$

where the probability of each galaxy in the sample is defined as:

$$P(L_i|\alpha, \beta, L^*) = \left[\frac{\int_{L_{\rm min}}^{\infty} \phi(L') \times F(L'; L_i, \sigma_i) dL'}{\int_{L_{\rm min}}^{\infty} \phi(L) dL}\right]^{w_i}. \quad (9)$$

In measuring the probability for each galaxy the normalization factor ϕ^* cancels out and at each luminosity (L_i) this probability can be measured by the three parameters α, β, and L^*. Equation (9) is a modified version of what was used in the original STY. Here we account for both incompleteness in the sample and line uncertainties of each galaxy. We account for incompleteness in the sample by including weights (w_i) into Equation (9). These weights are the inverse of the completeness at each luminosity with the simple idea that galaxies with the same luminosity at the same distance should have the same probability of being found. This is similar to incompleteness corrections in spectroscopic samples (see for example Zucca et al. 1994). The uncertainties in [C II] line luminosity estimates are taken into account by adding the error function ($F(L'; L_i, \sigma_i)$) to the probabilities. This is done by assuming a normal distribution for luminosities with 1σ errors as the width of the distribution and summing over all luminosities. While this is negligible for *Herschel*-detected GOALS sources which have small error bars, it is essential for the rest of the sample. This factor is in essence similar to what was introduced in Chen et al. (2003) for accounting for photometric redshift errors.

In practice, we need to vary parameters L^*, α, and β to find the maximum $\mathcal{L}$ as well as the posterior distribution for each of the parameters. However, this is very computationally expensive for a large enough grid with multiple integration, three free parameters, and over 600 galaxies. Therefore, rather than measuring the probabilities over the whole grid, we perform a random walk Markov Chain Monte Carlo (MCMC) to derive the desired parameters and their uncertainties. To further speed up the calculations, we go to the logarithm space and use the summation of probabilities rather than multiplication to measure $\mathcal{L}$.

We run our MCMC program with 100,000 steps randomly chosen from the three-dimensional grid (L^*, α, and β). The step size in each parameter is not fixed and is drawn from normal distributions. We start by measuring the probabilities as described by Equation (9) with an initial guess for the parameters. These initial guesses do not need to be precise as the first 5%–10% of steps are thrown away (burn-in process) and as long as the order of magnitude is correct the process will converge to the optimized values. At each step, with the jump to the new parameters we calculate the new $\mathcal{L}$ and compare it to the previous one. In addition, a random acceptance rate scheme is adopted, where the new parameters are accepted and added to the chain if the new likelihood is either larger than the previous one or if their ratio is larger than a random number drawn from a normal distribution. We choose the jump size (width of the normal distributions) to get an acceptance rate of 23%, which is shown theoretically to be the optimal value for an N-dimentional distribution (Roberts et al. 1997).

3.3. Results

Figure 3 represents our derived [C II] line luminosity function from both $1/V_{\rm max}$ (blue circles) and maximum likelihood estimator (solid cyan line) methods as well as the posterior distributions of α, β, and L^*. We also show on Figure 3 the estimated [C II] LF based on the GOALS measurements only without any completeness correction (purple squares) using the $1/V_{\rm max}$ method. It can be seen that while there is good agreement at the very bright end, the LF starts to be very incomplete and drops at luminosities below $\log 10(L_{\rm [C\,II]}) \sim 8.7$. This clarifies the importance of adding the estimated [C II] fluxes from the rest of the RBGS sample. We note here that the faintest and brightest [C II] emitters in the sample are from the GOALS galaxies with *Herschel* PACS observations and by including the rest of the RBGS sample we did not extrapolate to fainter or brighter [C II] luminosities.

The maximum likelihood curve (solid cyan line) is calculated from skewed Gaussian function fits to the posterior distributions with best-fitted parameters shown in Table 1. As can be seen from the figure, there is a good agreement within uncertainties between the maximum likelihood estimator and the $1/V_{\rm max}$ methods. In the maximum likelihood estimator method we accounted for sources that might be missing using our derived completeness function, in which we assigned random far-IR color to hundreds of galaxies at each [C II] luminosity and distance to determine whether they will be detected by our survey. We note that we have drawn the random far-IR colors from a uniform distribution in the color range of our sample due to lack of prior knowledge of the true distribution of sources that we might be missing. The agreement between the two methods of measuring the luminosity function demonstrates the validity of this assumption.

Our completeness simulation is designed to account for potential [C II] emitters that might be missed due to having $S_{60\,\mu{\rm m}}$ less than the flux limit of the RBGS sample. However, we have assumed similar far-IR color and dust temperature properties for the galaxies in this simulation to those in the RBGS sample. An important question is whether there exist galaxies with vastly different properties that could change our results. Many recent studies have shown the important role of dwarf galaxies in understanding how galaxies form and evolve in general (e.g., Dekel & Silk 1986; Ferguson & Binggeli 1994, Walter et al. 2007; Tolstoy et al. 2009). More specifically, studies of optical and UV luminosity functions found that dwarf galaxies can contribute significantly to the faint end of the luminosity function (e.g., Liu et al. 2008; Alavi et al. 2016). Madden et al. (2013), using *Herschel*, provides a rich far-IR

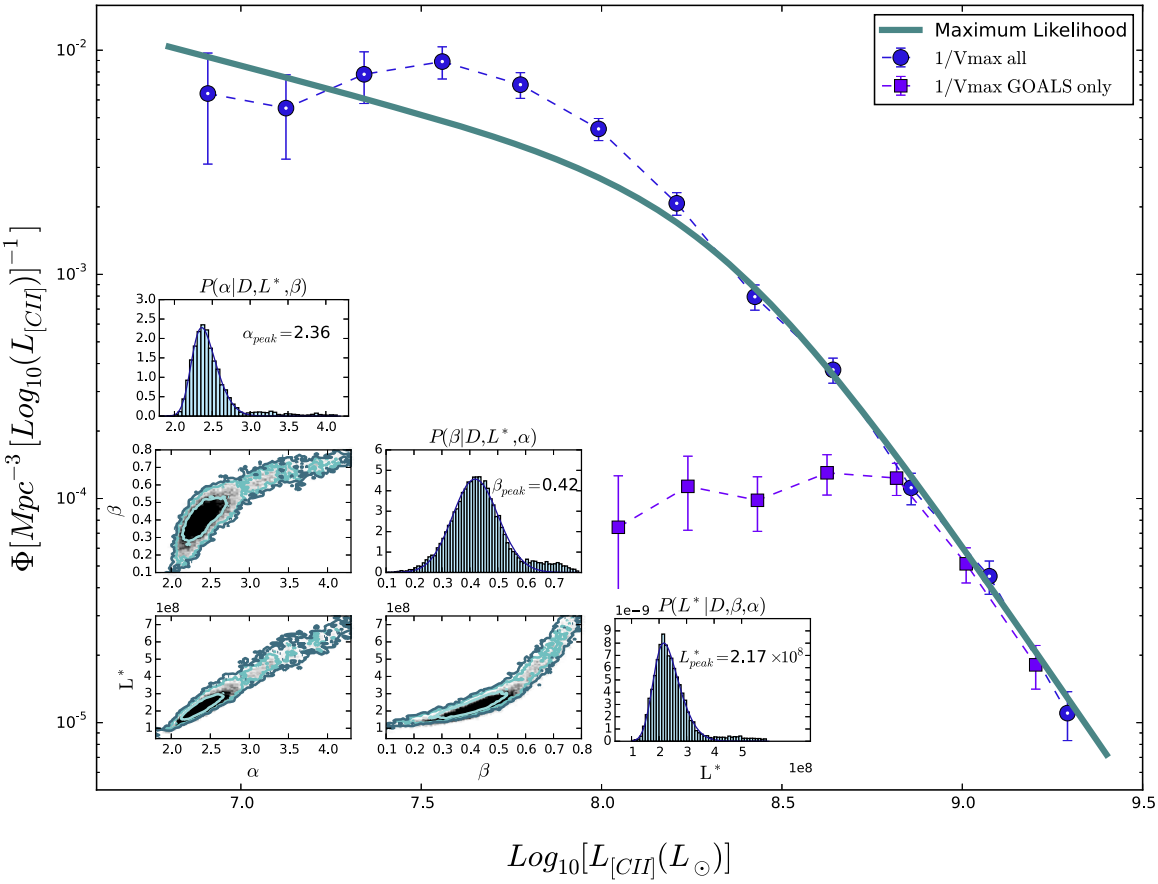

Figure 3. The [C II] line luminosity function. Blue circles are measured from the $1/V_{\rm max}$ method including all galaxies in the sample. Purple squares are measured from the $1/V_{\rm max}$ using only the GOALS galaxies with no extra correction. The cyan solid line is our estimate from the MCMC code based on the modified STY maximum likelihood estimator. The inset on the left corner show the 2D and 1D posterior distribution of α, β, and L^*. 1σ, 2σ, and 3σ confidence contours are plotted on the 2D distributions with solid blue lines.

and submm photometric and spectroscopic database for local dwarf galaxies covering a large range in metallicity (Dwarf Galaxy Survey—DGS). Focusing on the *Herschel* PACS spectroscopic data of the DGS, Cormier et al. (2015) found an increasing trend of [C II] luminosity with increased metallicity among the dwarfs, where they cover a large range of [C II] luminosites ($10^{4-9}\,L_\odot$) and metallicities ($1/50$–$1\,Z_\odot$). The low-metallicity dwarfs which have low [C II] luminosities have different dust temperature and far-IR colors compared to normal local galaxies (see Rémy-Ruyer et al. 2015). As we are only constraining the [C II] luminosity function down to $\sim 10^7\,L_\odot$, the dwarf population in that [C II] luminosity regime will not have low metallicities ($12 + \log(\mathrm{O/H}) > \sim 8.0$). These galaxies have similar far-IR colors and dust temperatures as the galaxies in our sample and therefore are taken care of in the completeness measurement. However, low-metallicity dwarf galaxies need to be taken into account if the [C II] luminosity function extends to very faint [C II] luminosities and they can play an important role in constraining the very faint end of the [C II] luminosity function.

4. DISCUSSION

Here, we compare our derived luminosity function to different local estimates obtained from other indirect diagnostics in the left panel of Figure 4.

First, we compare our derived [C II] luminosity function to an estimate based on the IR luminosity function and assuming fixed [C II]/FIR ratios. For this comparison, we use the IR luminosity function of Sanders et al. (2003) derived from the RBGS sample. We also take into account an extra factor to convert the total IR luminosity function to the far-IR luminosity function ($L_{\rm IR}/L_{\rm FIR} \sim 1.3$, Chapin et al. 2009). We note here that the IR luminosity function from Chapin et al. (2009) matches exactly the total IR luminosity function from Sanders et al. (2003). The gray shaded region in the left panel of Figure 4 corresponds to the range of [C II]/FIR = [0.0002–0.02] based on the scatter from Díaz-Santos et al. (2013). We also show data points from the PEP/HerMES (Gruppioni et al. 2013) local IR luminosity function assuming a fixed ratio of [C II]/FIR = 0.004 with gray squares, which is chosen to match the [C II] luminosity function. While fixing the [C II]/FIR ratio to a single value can result in good agreement between the IR and [C II] luminosity function, it is well known that not all galaxies can be described with a single value of [C II]/FIR. As previously shown in the literature (e.g., Díaz-Santos et al. 2013, 2014; Lutz et al. 2016), far-IR color and far-IR surface brightness are among the most important observables linked to the variation of [C II]/FIR, where the large variation is mostly among galaxies with hotter far-IR SEDs (see Figure 1). We note that converting the existing IR LF into the [C II] LF using a constant ratio has serious flaws because the [C II]/FIR ratio is not a constant number. For instance, low-luminosity galaxies could have stronger [C II] emission, whereas IR brighter ULIRGs/QSOs may have less. This could

Table 1
[C II] Luminosity Function Parameters

Method	α	β	$L^*(L_\odot) \times 10^8$	$\phi^*(\mathrm{Mpc}^{-3}\log_{10}(L_{[\mathrm{C\,II}]})^{-1})$
Maximum Likelihood	2.36 ± 0.25	0.42 ± 0.09	2.173 ± 0.743	0.003 ± 0.002

cause the shape of [C II] LF to significantly differ from that of the far-IR LF. We caution that such a simple LF conversion is extremely crude, as illustrated by the large shaded gray area.

Besides the [C II] atomic fine structure line, the rotational transitions of common interstellar molecules, predominantly carbon monoxide (CO), have been used in the literature extensively to study the cool gas content of galaxies. While the [C II] line is much stronger than the CO(1-0) molecular line, an apparent linear correlation between [C II] and CO(1-0) intensity is reported in galactic star-forming regions as well as starburst extragalactic sources (e.g., Crawford et al. 1985; Wolfire et al. 1989; Stacey et al. 1991). We take the CO(1-0) local luminosity function of Keres et al. (2003) and convert it to an estimate of [C II] luminosity function shown on the left panel of Figure 4 in light blue. Here, we assumed a range of $\log([\mathrm{C\,II}]/\mathrm{CO}) = 2.5$–$4.5$ based on the lowest and highest values presented in Stacey et al. (1991) for the galaxies NGC 660 and LMC30Dor respectively (a similar range is observed by Hailey-Dunsheath et al. 2010). Stacey et al. (1991) showed that more active normal starburst galaxies have $L_{[\mathrm{C\,II}]}/L_{\mathrm{CO}}$ of ~4000, while more quiescent spiral galaxies have a factor of 2 lower ratios. The dashed blue line is derived if a fixed value of $\log([\mathrm{C\,II}]/\mathrm{CO}) = 3.8$ corresponding to the average ratio reported by Stacey et al. (1991) is assumed. Madden (2000) also measured the $L_{[\mathrm{C\,II}]}/L_{\mathrm{CO}}$ for local low-luminosity dwarfs and showed that the ratio can get as high as ~80,000. As can be seen from the figure, assuming the fixed average ratio reported by Stacey et al. (1991) yields a good agreement between the two luminosity functions at faint ends but the discrepancy gets larger as one moves to the brighter [C II] luminosities. While some difference can be partly due to the completeness correction applied in deriving the CO(1-0) luminosity function, as well as forcing a Schechter functional form fit, the large uncertainty is from the ratio of the lines. A better agreement between the two can be achieved if a CO-dependent ratio of $\log([\mathrm{C\,II}]/\mathrm{CO})$ is applied to the CO luminosity function where galaxies with higher CO luminosity have lower [C II]/CO ratio compared to those with lower CO luminosity. Theoretically this might be explained by CO being photodissociated into C and C^+ in low dust and metallicity environments by a strong far-UV field from young stars (e.g., Wolfire et al. 2010; Madden et al. 2013).

In Figure 4 (left panel) we also compare our luminosity function measurement to the recent estimate of Popping et al. (2016) using semi-analytic models (SAMs) and radiative transfer models (magenta dashed line). Popping et al. (2016) studied the evolution of both CO and [C II] luminosity functions from $z = 0$–6. However, their models under-predict the local [C II] luminosity of far-IR-bright galaxies (Figure 3 of Popping et al. 2016) which explains the very large disagreement in the bright end seen here. Gruppioni et al. (2015) compared the star formation rate function derived from IR luminosity with those derived from four different SAMs and found a similar trend at higher redshifts ($z \sim 2$). Similar disagreement has also been reported between the SAMs and the bright end of the CO luminosity function by Vallini et al. (2016). There, they suggest that the SAMs' difficulty in modeling the AGN feedback that affects the inflow/outflow of gas in the largest and most massive galaxies might explain the reason for this difference. Regardless of the shape of the luminosity function at $z = 0$, their models predict that the number density of [C II] line-emitting galaxies increases from $z = 6$ to $z = 4$, remains relatively constant until $z = 1$, and rapidly decreases toward $z = 0$.

4.1. Redshift Evolution

Understanding the precise evolution of the [C II] luminosity function would require a larger sample of high-redshift galaxies than already exists. ALMA with full capability is ideal for acquiring such a statistical sample. There however exists limited observations and limited high-redshift [C II] detections (e.g., Swinbank et al. 2012; Capak et al. 2015; Matsuda et al. 2015). We show on the right panel of Figure 4 where these measurements sit as well as a very rough estimate of the [C II] luminosity function at high redshifts based on the UV and IR observations.

The cyan circle on the right panel of Figure 4 represents a lower limit from the ALMA detection of [C II] in two $z \sim 4$ galaxies by Swinbank et al. (2012). In that study, they suggested a dramatic increase from $z = 0$ to $z = 4$ in the number density at the bright end of the luminosity function in contrast to what we see here. This is solely due to their lower number density estimate at the bright end of [C II] luminosity function at $z = 0$. To estimate the $z = 0$ luminosity function Swinbank et al. (2012) used the Sanders et al. (2003) far-IR luminosity function and the [C II]/FIR with far-IR luminosity correlation of Brauher et al. (2008). To test the reliability of their method they also used [C II] luminosities of 227 galaxies compiled by Brauher et al. (2008). As the data come from a complex mix of observations, completeness measurement becomes a big issue.

Using ALMA cycle 1 archival data (in band 7), Matsuda et al. (2015) looked for [C II] emission in $z \sim 4$ galaxies and found no significant emission. They presented upper limits to the $z = 4$ [C II] luminosity function which is at least two orders of magnitude larger than the [C II] luminosity function expected from the UV luminosity function. Capak et al. (2015) observed nine $z \sim 5$ normal (~ 1–$4L_*$) star-forming galaxies using ALMA and detected [C II] in all of them. They reported enhancement in the [C II] emission relative to the far-IR continuum and therefore a strong evolution in the ISM properties in the very early universe. Blue circles on the right panel of Figure 4 represent a very rough estimate of where these measurements sit compared to the local luminosity function. To do this, we measure the volume for each observation using the area and the redshift width of each ALMA pointing and, as this was a targeted observation of Lyman break galaxies (LBGs), we correct the volume using the number density of these galaxies (Bouwens et al. 2015). Aside from these factors and the low number statistics which make these estimates very sensitive on choice of bins and therefore uncertain, it should be noted that there might exist classes of

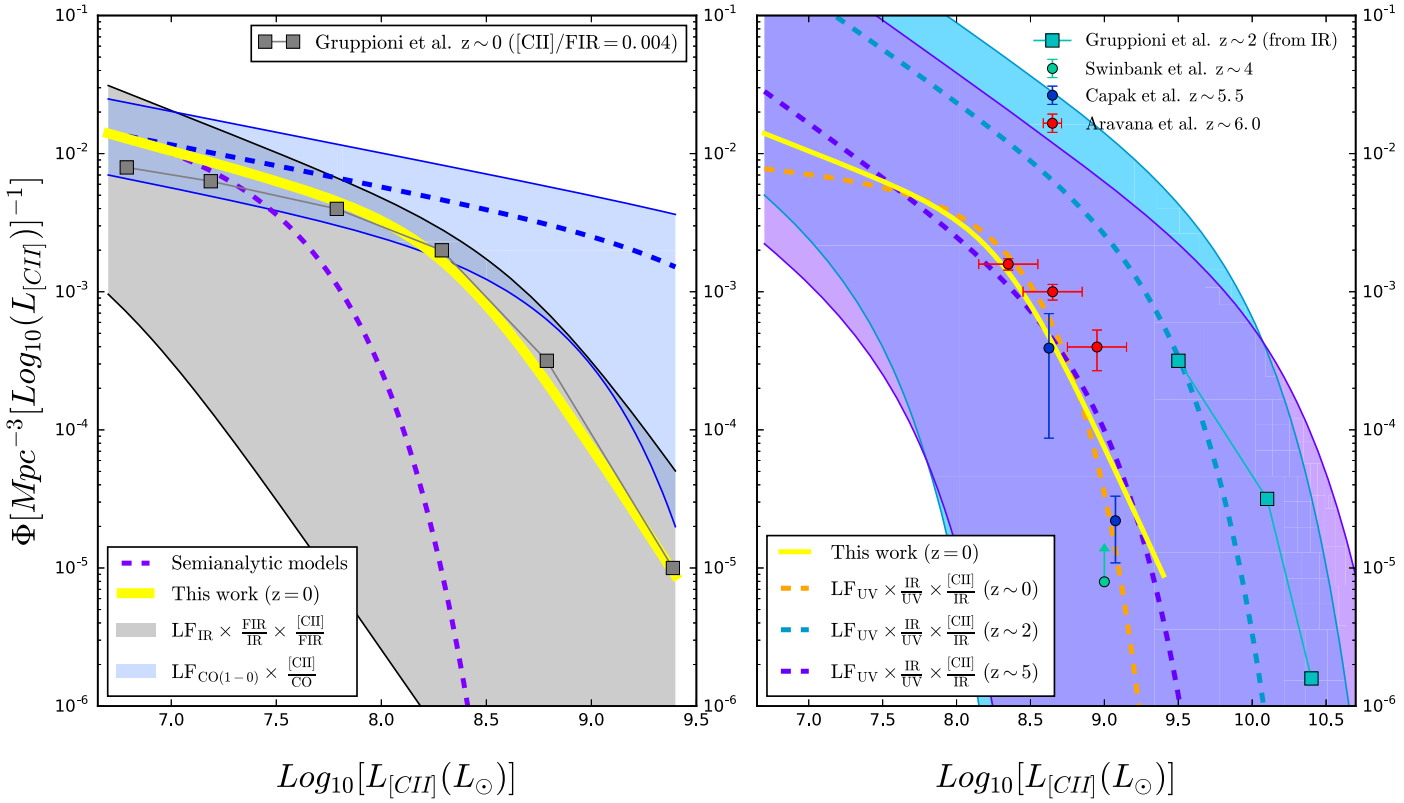

Figure 4. Comparison of the derived [C II] line luminosity function (solid yellow line) with other indirect estimates. Left: conversion of IR luminosity function (Sanders et al. 2003) to [C II] line luminosity function assuming a range of [C II]/FIR shown as the gray shaded region. Gruppioni et al. (2013) local measurements of IR luminosity function are plotted for comparison (gray squares) assuming a fixed ratio of 0.004 in [C II]/FIR. The conversion of the CO(1-0) luminosity function (Keres et al. 2003) to [C II] LF is shown as the light blue shaded region with the range adopted from Stacey et al. (1991) and the blue dashed line represents a fixed value of log([C II]/CO) = 3.8. The purple dashed line shows the [C II] luminosity function prediction from Popping et al. (2016) based on semi-analytic models and radiative transfer codes. Right: prediction of evolution with redshift. The orange dashed line shows the $z \sim 0$, the blue dashed line and shaded region represent $z \sim 2$ and the purple dashed line and shaded region show $z \sim 5$ based on UV observations with UV luminosity functions adopted from Wyder et al. (2005), Alavi et al. (2014), and Bouwens et al. (2015), respectively. The green limit is from Swinbank et al. (2012) at $z \sim 4$ and the dark blue data points are estimates from Capak et al. (2015) at $z \sim 5$. Also shown on the plot is the [C II] luminosity function estimate based on Gruppioni et al. (2013) $z \sim 2$ IR luminosity function (cyan squares).

Table 2
$1/V_{\rm max}$ Determination of the Local [C II] Luminosity Funcition

$\rm Log_{10}(L_{[C\ II]}(L_\odot))$	$\Phi[\rm Mpc^{-3}[Log_{10}(L_{[C\ II]})]^{-1}]$
6.9	0.00598 ± 0.003456
7.1	0.01119 ± 0.003633
7.3	0.00673 ± 0.0019
7.5	0.00804 ± 0.001463
7.7	0.00764 ± 0.001041
7.9	0.00532 ± 0.000599
8.2	0.00225 ± 0.000276
8.4	0.00117 ± 0.000138
8.6	0.00044 ± 5.8e–05
8.8	0.00016 ± 2.3e–05
9.0	6e–05 ± 1e–05
9.2	2e–05 ± 4e–06

galaxies that are faint in the UV and optical and therefore not selected as LBGs at high redshifts that are bright in the far-IR and can contribute to the luminosity function of the [C II] line. Recently, Aravena et al. (2016) identified 14 [C II] line-emitting candidates using ALMA observations of optical dropout galaxies in the Hubble Ultra-Deep Field in the range $6 < z < 8$. Their data points are overplotted on the right panel of Figure 4.

Also shown on the right panel of Figure 4 are estimates of [C II] luminosity function from UV observations at three different redshifts ($z = 0$, 2, and 5). As a crude estimate, we start with the UV luminosity function, and we adopt the values and uncertainties from Wyder et al. (2005) for local galaxies, from Alavi et al. (2014) at $z = 2$ and from Bouwens et al. (2015) at $z = 5$. To convert this to an IR estimate we use the IRX–β relation (Meurer et al. 1999), which states that the ratio of dust emission in the IR to UV emission (IRX) correlates with the UV spectral slope β. We chose the ratio from the literature (Takeuchi et al. 2012; Alavi et al. 2014; Capak et al. 2015) at each redshift based on the reported average β value and the best corresponding IRX–β curve (i.e., Calzetti-like dust (Calzetti et al. 2000) for $z = 0$, 2 and SMC-like dust (Gordon et al. 2003) for $z = 5$). These correspond to $\log(L_{\rm IR}/L_{1600})$ of 1.0, 0.7, and −0.2 for $z = 0$, 2, and 5 respectively. The final factor is an assumption for the [C II]/IR ratio which yields an estimate of the [C II] luminosity function. Again this average ratio and its range are taken from the literature to be 0.01 [0.001–0.03] at $z = 2$ (Stacey et al. 2010) and 0.01 [0.003–0.03] at $z = 5$ (Capak et al. 2015). At $z = 0$ (orange dashed line) we only show the average curve to compare with our derived local [C II] luminosity function. Overall the agreement between the UV estimate and the actual derived [C II] luminosity function is good despite all the assumptions that went into the estimate from the UV. At $z = 2$ ($z = 5$), the cyan (purple) dashed line shows the estimated [C II] luminosity function with the median assumptions and the cyan (purple)

shaded region corresponds to the whole possible range based on errors of the UV luminosity function, the IR/UV, and the [C II]/IR. As can be seen from the width of the shaded regions, these are very uncertain estimates and ALMA observations are needed to constrain the picture. However, assuming the median values (dashed lines) we see a similar evolutionary trend as predicted by Popping et al. (2016) simulations, where the high redshift and local estimates are similar and the rise in the number densities is seen at intermediate redshifts ($z \sim 2$).

IR luminosity functions can exclude the uncertainy from the IRX–β but, unfortunately, at high redshifts ($z > 3$) they only overlap with the brightest part of our [C II] luminosity function. For example, Gruppioni et al. (2013), using *Herschel* PACS-selected galaxies, estimated the IR luminosity function out to $z = 4$, but their highest redshift bins only cover [C II] luminosities outside the range of our study. However, we use their IR luminosity function at $z = 0$ and $z = 2$ and again assume a [C II]/IR ratio (as in our UV test above) and find perfect agreement for the local measurement and agreement within the errors at $z = 2$. These estimates of the [C II] luminosity function are shown on Figure 4 with gray squares on the left panel at $z = 0$ and at $z = 2$ with cyan squares on the right panel.

In conclusion, we find tentative evidence which suggests that redshift evolution of [C II] LF may not be simply linear. The volume density of [C II] emitters may increase significantly from $z = 0$ to $z = 2$, but at $z = 5$–6, [C II] LF seems to return back to the similar level as $z = 0$. This redshift evolution behavior is similar to that of the cosmic star formation rate density which rises from early epochs to its peak value between $z \sim 3$ and 1 and drops toward the present time (e.g., Hopkins & Beacom 2006; Khostovan et al. 2015). This evolution of the cosmic star formation rate density is partly explained by the ISM masses and the accretion/consumption of the molecular/total gas (e.g., Walter et al. 2014; Genzel et al. 2015; Scoville et al. 2016).

5. SUMMARY

In this paper we presented for the first time, the local [C II] emission line luminosity function using both *Herschel* PACS-observed emission line data from the GOALS survey as well as estimates based on the far-IR emission for the rest of the RBGS galaxies. This sample of 596 galaxies covers 91.3% of the entire sky (37,657 deg^2) and is complete at $S_{60\,\mu m} > 5.24$ Jy. We argue that in the absence of a blind, deep [C II] flux-limited survey, this is the best approach for estimating the local [C II] luminosity function.

1. Here, the luminosity function is estimated using both the $1/V_{max}$ and the STY maximum likelihood approach over the [C II] luminosity range $\sim 10^{7-9}$. The incompleteness function is measured over a grid of [C II] luminosity and distance by assigning hundreds of far-IR colors to each cell in the grid and recovering the $S_{60\,\mu m}$ flux density, to calculate the fraction of objects that could end up in the final sample at each [C II] luminosity and distance. We find that for the majority of the sample the completeness is more than 80%. We also showed that low-metallicity dwarf galaxies would not affect our [C II] luminosity function in the range of [C II] luminosities covered by this work, but should be taken into account if the luminosity function is to be extended to fainter [C II] luminosities.
2. We compared our derived luminosity function with the far-IR luminosity functions from the literature. The [C II]/FIR ratio is not a single value for different galaxies and it varies with the average dust temperature covering the range ~0.0002–0.02. We show that our derived [C II] luminosity function lies in the range defined by the [C II]/FIR ratio and has a similar shape as the far-IR luminosity function.
3. The [C II] luminosity function derived from the SAMs and radiative transfer models (Popping et al. 2016) deviates from our luminosity function, and the disagreement gets larger at the bright end.
4. We also compared the local CO(1-0) luminosity function of Keres et al. (2003), to our [C II] luminosity function assuming a range of log([C II]/CO) = 2.5–4.5 from the literature and found that for the two luminosity functions to agree the [C II]/CO value should be larger at fainter CO luminosities.
5. ALMA with full capability will be ideal to acquire large samples of high-redshift [C II] emitters. While now there are only limited detections and therefore large uncertainty, we predict an evolution in the [C II] luminosity function similar to that of the star formation rate density. We show that there are indications that the number density of [C II] emitters would increase from early times ($z \sim 5$) to its maximum value at $z \sim 2$ and decrease again to the present time.

We wish to thank the referee for helpful comments which improved the content and presentation of this paper. SH wishes to thank Iary Davidzon and Hooshang Nayyeri for very useful discussions. AF acknowledges support from the Swiss National Science Foundation. T.D.-S. acknowledges support from ALMA-CONICYT project 31130005 and FONDECYT regular project 1151239.

REFERENCES

Alavi, A., Siana, B., Richard, J., et al. 2014, ApJ, 780, 143
Alavi, A., Siana, B., Richard, J., et al. 2016, ApJ, 832, 56
Aravena, M., Decarli, R., Walter, F., et al. 2016, ApJ, 833, 71
Armus, L., Mazzarella, J. M., Evans, A. S., et al. 2009, PASP, 121, 559
Boselli, A., Gavazzi, G., Lequeux, J., & Pierini, D. 2002, A&A, 385, 454
Bouwens, R. J., Illingworth, G. D., Oesch, P. A., et al. 2015, ApJ, 803, 34
Brauher, J. R., Dale, D. A., & Helou, G. 2008, ApJS, 178, 280
Brisbin, D., Ferkinhoff, C., Nikola, T., et al. 2015, ApJ, 799, 13
Calzetti, D., Armus, L., Bohlin, R. C., et al. 2000, ApJ, 533, 682
Capak, P. L., Carilli, C., Jones, G., et al. 2015, Natur, 522, 455
Carilli, C. L., & Walter, F. 2013, ARA&A, 51, 105
Chapin, E. L., Hughes, D. H., & Aretxaga, I. 2009, MNRAS, 393, 653
Chen, H.-W., Marzke, R. O., McCarthy, P. J., et al. 2003, ApJ, 586, 745
Cormier, D., Lebouteiller, V., Madden, S. C., et al. 2012, A&A, 548, A20
Cormier, D., Madden, S. C., Lebouteiller, V., et al. 2015, A&A, 578, A53
Crawford, M. K., Genzel, R., Townes, C. H., & Watson, D. M. 1985, ApJ, 291, 755
Decarli, R., Walter, F., Carilli, C., et al. 2014, ApJL, 782, L17
Dekel, A., & Silk, J. 1986, ApJ, 303, 39
De Looze, I., Cormier, D., Lebouteiller, V., et al. 2014, A&A, 568, A62
Díaz-Santos, T., Armus, L., Charmandaris, V., et al. 2013, ApJ, 774, 68
Díaz-Santos, T., Armus, L., Charmandaris, V., et al. 2014, ApJL, 788, L17
Farrah, D., Lebouteiller, V., Spoon, H. W. W., et al. 2013, ApJ, 776, 38
Felten, J. E. 1976, ApJ, 207, 700
Ferguson, H. C., & Binggeli, B. 1994, A&ARv, 6, 67
Genzel, R., Tacconi, L. J., Lutz, D., et al. 2015, ApJ, 800, 20
Goldsmith, P. F., Langer, W. D., Pineda, J. L., & Velusamy, T. 2012, ApJS, 203, 13
Goldsmith, P. F., Yıldız, U. A., Langer, W. D., & Pineda, J. L. 2015, ApJ, 814, 133

Gordon, K. D., Clayton, G. C., Misselt, K. A., Landolt, A. U., & Wolff, M. J. 2003, ApJ, 594, 279
Graciá-Carpio, J., Sturm, E., Hailey-Dunsheath, S., et al. 2011, ApJL, 728, L7
Gruppioni, C., Calura, F., Pozzi, F., et al. 2015, MNRAS, 451, 3419
Gruppioni, C., Pozzi, F., Rodighiero, G., et al. 2013, MNRAS, 436, 2875
Gullberg, B., De Breuck, C., Vieira, J. D., et al. 2015, MNRAS, 449, 2883
Hailey-Dunsheath, S., Nikola, T., Stacey, G. J., et al. 2010, ApJL, 714, L162
Hayes, M. A., & Nussbaumer, H. 1984, A&A, 139, 233
Helou, G., Lu, N. Y., Werner, M. W., Malhotra, S., & Silbermann, N. 2000, ApJL, 532, L21
Herrera-Camus, R., Bolatto, A. D., Wolfire, M. G., et al. 2015, ApJ, 800, 1
Hogg, D. W. 1999, arXiv:astro-ph/9905116
Hopkins, A. M., & Beacom, J. F. 2006, ApJ, 651, 142
Kaufman, M. J., Wolfire, M. G., Hollenbach, D. J., & Luhman, M. L. 1999, ApJ, 527, 795
Kennicutt, R. C., Calzetti, D., Aniano, G., et al. 2011, PASP, 123, 1347
Keres, D., Yun, M. S., & Young, J. S. 2003, ApJ, 582, 659
Khostovan, A. A., Sobral, D., Mobasher, B., et al. 2015, MNRAS, 452, 3948
Liu, C. T., Capak, P., Mobasher, B., et al. 2008, ApJ, 672, 198
Lutz, D., Berta, S., Contursi, A., et al. 2016, A&A, 591, A136
Madden, S. C. 2000, NewAR, 44, 249
Madden, S. C., Rémy-Ruyer, A., Galametz, M., et al. 2013, PASP, 125, 600
Malhotra, S., Helou, G., Stacey, G., et al. 1997, ApJL, 491, L27
Malhotra, S., Kaufman, M. J., Hollenbach, D., et al. 2001, ApJ, 561, 766
Matsuda, Y., Nagao, T., Iono, D., et al. 2015, MNRAS, 451, 1141
Meurer, G. R., Heckman, T. M., & Calzetti, D. 1999, ApJ, 521, 64
Nagao, T., Maiolino, R., De Breuck, C., et al. 2012, A&A, 542, L34
Olsen, K. P., Greve, T. R., Narayanan, D., et al. 2015, ApJ, 814, 76
Patel, H., Clements, D. L., Vaccari, M., et al. 2013, MNRAS, 428, 291
Pilbratt, G. L., Riedinger, J. R., Passvogel, T., et al. 2010, A&A, 518, L1
Pineda, J. L., Langer, W. D., & Goldsmith, P. F. 2014, A&A, 570, A121
Poglitsch, A., Waelkens, C., Geis, N., et al. 2010, A&A, 518, L2
Popping, G., van Kampen, E., Decarli, R., et al. 2016, MNRAS, 461, 93
Press, W. H., & Schechter, P. 1974, ApJ, 187, 425
Rémy-Ruyer, A., Madden, S. C., Galliano, F., et al. 2015, A&A, 582, A121
Roberts, G. O., Gelman, A., & Gilks, W. R. 1997, Ann. Appl. Probab., 7, 110
Sandage, A., Tammann, G. A., & Yahil, A. 1979, ApJ, 232, 352
Sanders, D. B., Mazzarella, J. M., Kim, D.-C., Surace, J. A., & Soifer, B. T. 2003, AJ, 126, 1607
Sargsyan, L., Lebouteiller, V., Weedman, D., et al. 2012, ApJ, 755, 171
Schechter, P. 1976, ApJ, 203, 297
Schmidt, M. 1968, ApJ, 151, 393
Scoville, N., Sheth, K., Aussel, H., et al. 2016, ApJ, 820, 83
Soifer, B. T., Sanders, D. B., Madore, B. F., et al. 1987, ApJ, 320, 238
Stacey, G. J., Geis, N., Genzel, R., et al. 1991, ApJ, 373, 423
Stacey, G. J., Hailey-Dunsheath, S., Ferkinhoff, C., et al. 2010, ApJ, 724, 957
Swinbank, A. M., Karim, A., Smail, I., et al. 2012, MNRAS, 427, 1066
Takeuchi, T. T., Yuan, F.-T., Ikeyama, A., Murata, K. L., & Inoue, A. K. 2012, ApJ, 755, 144
Tolstoy, E., Hill, V., & Tosi, M. 2009, ARA&A, 47, 371
Vallini, L., Gallerani, S., Ferrara, A., Pallottini, A., & Yue, B. 2015, ApJ, 813, 36
Vallini, L., Gruppioni, C., Pozzi, F., Vignali, C., & Zamorani, G. 2016, MNRAS, 456, L40
Walter, F., Cannon, J. M., Roussel, H., et al. 2007, ApJ, 661, 102
Walter, F., Decarli, R., Sargent, M., et al. 2014, ApJ, 782, 79
Wolfire, M. G., Hollenbach, D., & McKee, C. F. 2010, ApJ, 716, 1191
Wolfire, M. G., Hollenbach, D., & Tielens, A. G. G. M. 1989, ApJ, 344, 770
Wyder, T. K., Treyer, M. A., Milliard, B., et al. 2005, ApJL, 619, L15
Zucca, E., Pozzetti, L., & Zamorani, G. 1994, MNRAS, 269 arXiv:astro-ph/9403063